https://doi.org/10.15407/ufm.24.04.715

P.E. MARKOVSKY [1,*], D.V. KOVALCHUK [1,2], S.V. AKHONIN [3], S.L. SCHWAB [3], D.G. SAVVAKIN [1,], O.O. STASIUK [1,***], D.V. ORYSHYCH [1], D.V. VEDEL [4], M.A. SKORYK [1], and V.P. TKACHUK [1,2]**

[1] G.V. Kurdyumov Institute for Metal Physics of the N.A.S. of Ukraine, 36 Acad. Vernadsky Boulevard, UA-03142 Kyiv, Ukraine
[2] JSC NVO 'Chervona Hvylya', 28 Dubrovitska Str., UA-04114 Kyiv, Ukraine
[3] E.O. Paton Electric Welding Institute of the N.A.S. of Ukraine, 11, Kazymyr Malevych Str., UA-03150 Kyiv, Ukraine
[4] I.M. Frantsevych Institute for Problems of Materials Science of the N.A.S. of Ukraine, 3 Omeljan Pritsak Str., UA-03142 Kyiv, Ukraine

* pmark@imp.kiev.ua, ** savva@imp.kiev.ua, *** olek.stasiuk@gmail.com

NEW APPROACH FOR MANUFACTURING Ti–6Al–4V + 40%TiC METAL-MATRIX COMPOSITES BY 3*D* PRINTING USING CONIC ELECTRON BEAM AND CORED WIRE. PT. 1: MAIN FEATURES OF THE PROCESS, MICROSTRUCTURE FORMATION AND BASIC CHARACTERISTICS OF 3*D* PRINTED MATERIAL

In this paper, a new approach for additive manufacturing metal-matrix composites based on Ti–6Al–4V titanium alloy reinforced with titanium carbide particles, as

Citation: P.E. Markovsky, D.V. Kovalchuk, S.V. Akhonin, S.L. Schwab, D.G. Savvakin, O.O. Stasiuk, D.V. Oryshych, D.V. Vedel, M.A. Skoryk, and V.P. Tkachuk, New Approach for Manufacturing Ti–6Al–4V+40% TiC Metal-Matrix Composites by 3*D* Printing Using Conic Electron Beam and Cored Wire. Pt. 1: Main Features of the Process, Microstructure Formation and Basic Characteristics of 3*D* Printed Material, *Progress in Physics of Metals*, **24**, No. 4: 715–740 (2023)

well as layered structures consisted of such composite and Ti–6Al–4V alloy layers is considered. The approach is based on 3*D* printing with a conical electron beam using a special cored wire, whose composition corresponds to metal-matrix composite. The issues of production such a wire, the features of the 3*D* printing process, when using it, as well as the features of formation of the microstructure and phase composition of the printed composite material are described. The issues of titanium-carbide particles' wetting with Ti–6Al–4V melt during process of 3*D* printing, as well as possible thermogravitational effects (floating or drowning) for solid TiC particles within the melt are considered in detail with additional experiments. The influence of individual components of the wire composition on the formation of the microstructure and its uniformity over the cross section of the printed layer is shown. The possibility of controlling the formation of homogeneous structural state and obtaining sufficiently high values of the hardness (of above 600 *HV*) of the metal-matrix composite layer printed on the Ti–6Al–4V baseplate is shown.

Keywords: additive manufacturing, 3*D* printing, titanium alloys, metal-matrix composite, microstructure, texture, hardness.

1. Ti-Based Metal-Matrix Composites and Manufacturing-Related Problematics

Lightweight and strong titanium-based materials are very attractive for various structural applications, especially taking into consideration their high ductility and excellent corrosion resistance [1–3]. However, restricting disadvantages of titanium alloys are their low hardness and insufficient wear resistance, which can be overcome by creation of titanium-based metal-matrix composites (MMCs) reinforced with hard high-modulus phases. It is commonly recognized, high-modulus and light titanium carbide (TiC) and titanium boride (TiB) particles are the most promising to reinforce titanium alloy matrix [4–6].

Such MMCs can be manufactured by various processing routes, including conventional ingot melting approach [4, 7], which may cause some specific changes in final composition due to reaction between titanium melt and hard particles [7, 8]. As a result of such interactions between charge materials and transformations of the phase composition, a relatively coarse cast microstructure with dendritic morphology of carbide phase can be formed, which has an extremely negative effect on the properties of such an MMC, being especially harmful for its plasticity [4, 7, 9]. Another approach is based on powder metallurgy technology that ensures much better dispersion and controlled uniformity of the final material [10–14]. However, since sintering of MMCs takes place at relatively high temperatures, the interaction of such a reactive metal as titanium with raw carbide or boride powder particles also takes place. Usually, titanium diboride TiB_2 raw powders are used in powder approaches, which transform into disperse monoboride TiB particles on high-temperature sintering following the solid-state reaction $2Ti + TiB_2 =$

= 2TiB [14, 15]. Titanium carbide TiC is a relatively stable compound, but at temperatures commonly used for sintering of powder compacts (above 1000 °C), active diffusion of carbon from raw TiC powder particles into surrounding titanium matrix occurs, which leads to formation of layers of intermediate composition around the carbide particles [7, 16]. Due to the differences in the transformations occurring during the sintering, MMCs reinforced by TiB and TiC differ in the microstructure dispersion of both the matrix and the strengthening particles, as well as in the residual porosity of the sintered materials. Sintered MMCs with TiB reinforcements are characterized with essentially finer all structural elements but increased porosity that results in drop of strength and in extremely brittleness, especially when the amount of TiB particles reaches 20 vol.% and more [13, 17]. At the same time, press-and-sinter approach ensures lower residual porosity of the MMCs reinforced by TiC, some coarsening of TiC particles and matrix grains, such microstructure features jointly result in minor plasticity [13]. If nearly dense material is achieved with additional operations like HIP or post-sintering hot deformation, MMCs with TiB reinforcements have some superiority in properties over MMCs reinforced with TiC. As shown in Ref. [16], there is a certain maximum allowable amount (40%) of introduced TiC particles in titanium-based matrix, at which maximal hardening effect is achieved. Higher TiC content hindered formation of matrix alloy from starting powder blend and led to increased porosity due to the interactions between the matrix and carbide particles during sintering, thus, the hardening effect decreased (Fig. 1).

Alternative to conventional ingot metallurgy and powder metallurgy manufacturing approaches are additive manufacturing technologies, which, due to a relatively small melting zone, provide some intermediate microstructural states between those obtained by cast and powder sintering methods [18–20]. Additive technologies, including 3*D* printing approach, have a great potential for cost-efficient manufacturing of near-net-shape metallic products, which is extremely important for titanium-based materials taking into account their relatively high cost compared to other construction materials like steels and aluminium alloys. In addition, this approach looks as very promising to produce various titanium-based MMCs. At the same time, achievement of desirable mechanical and other characteristics of 3*D* printed titanium-based products is a great challenge, requiring sustainable protection of molten metal from contamination and formation of desirable solidified microstructure because of multiple local melting and heat effects during layer-by-layer printing [21]. Therefore, there is a great interest for testing and adaptation of 3*D* printing methods to produce titanium-based MMCs products with desirable microstructure and characteristics. Present investigation is dedicated to achievement of this target.

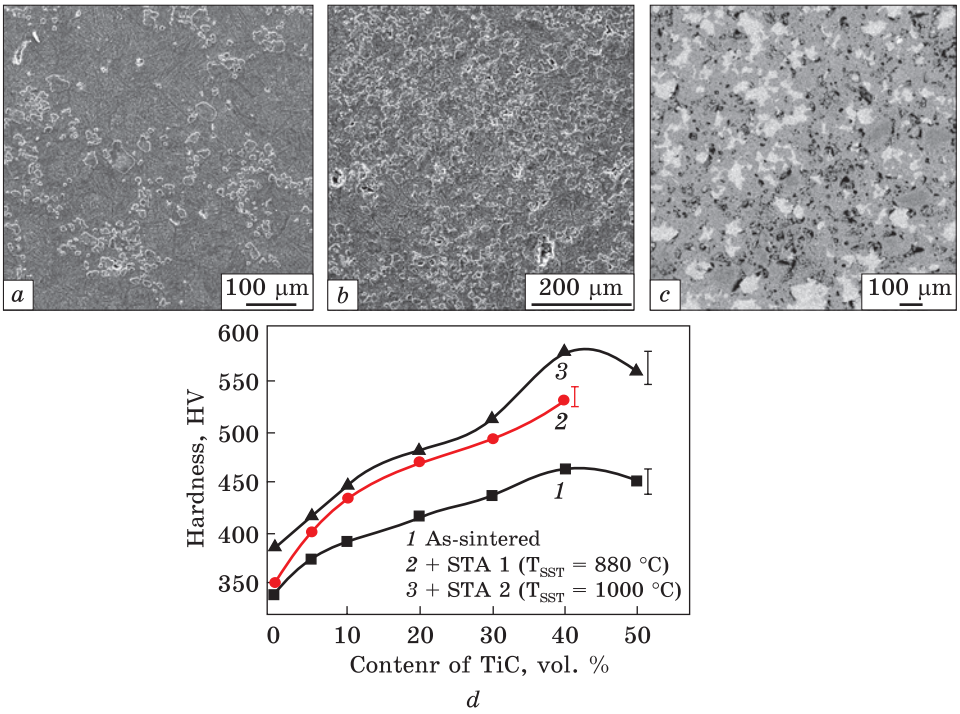

Fig. 1. Microstructure of Ti–6Al–4V+*X*% TiC MMCs with (*a*) 20, (*b*) 40, and (*c*) 50% TiC, and (*d*) influence of TiC content on hardness of MMCs. (*a*, *b*) SEM, SE, (*c*) SEM, BSE [16]

2. Features of the Advanced DED-Wire 3*D* Printing Method with a Profile Electron Beam and Coaxial Wire Feed

Advanced additive manufacturing (AM) technology called xBeam 3*D* Metal Printing developed by the company 'Chervona Hvylya' [22, 23] has already demonstrated the possibility of manufacturing products from titanium alloys with a controlled microstructure, stoichiometric chemical composition, and therefore the desired mechanical characteristics [24–31]. The key distinctive feature of the xBeam 3*D* Metal Printing compared to other DED-wire methods is the employing a profile electron beam in the form of a hollow inverted cone to create a melt pool on the substrate and melt the wire feedstock, which is fed coaxially with the said electron beam (Fig. 2). [25]. This configuration of the deposition zone, together with a moderate power concentration in the focus of such an electron beam, substantially reduces the total heat input during the deposition of added material and reduces temperature gradients in and around the deposition zone. This provides good control over the formation of the metal structure of the deposited material, in particular, preventing the formation of a coarse columnar structure typical for

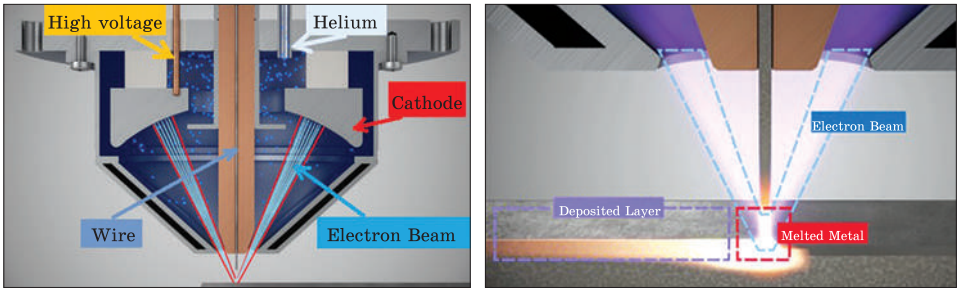

a *b*

Fig. 2. Configuration of the xBeam 3*D* Metal Printing process: (*a*) general configuration, and (*b*) configuration of distribution of the electron beam power in the deposition zone [26]

most metal AM methods. For example, it has already been demonstrated that the structure of the Ti–6Al–4V titanium alloy, obtained by the xBeam technology, when appropriate heat treatment is applied, can be comparable and even better than the structure of the wrought metal [25–29]. Accordingly, the mechanical properties of the 3*D* printed material also have good indicators that meet all related standards [28]. In addition, the essential advantages of this method over other technologies of 3*D* metal printing are the combination of high performance with high accuracy and low production cost, which, in particular, is ensured by using ordinary commercial wire as a feedstock.

Separately, it is worth noting that the possibility of coaxial feeding the feedstock with a profile-heating source, which surrounds the feedstock evenly from all sides, allows using a cored wire as a feedstock [23]. By definition, cored wire is a thin-walled metal tube filled with powder-like fillers necessary to form the required chemical composition. The use of cored wire must guarantee the reliable entry of all the powder into the melt pool on the surface to maintain the stoichiometry of the chemical composition. When using an electron beam as a heating source, it is critically important to avoid the direct impact of the electron beam on the powder from the cored wire to prevent electrostatic scattering of the powder in the vacuum. This can be ensured only by creating conditions where the powder enters the melt pool before the wire sheath, which protects the powder from the direct action of the electron beam, melts. Only the coaxial configuration of feeding the cored wire feedstock can create such conditions. However, this still requires the fulfilment of certain additional conditions, which will be discussed in the description of the experiment in the following sections.

Contrary to ductile titanium alloys, there is a great problem to produce wire made of relatively brittle titanium-based MMC using standard approach based on hot rolling, drawing or extrusion operations. That is

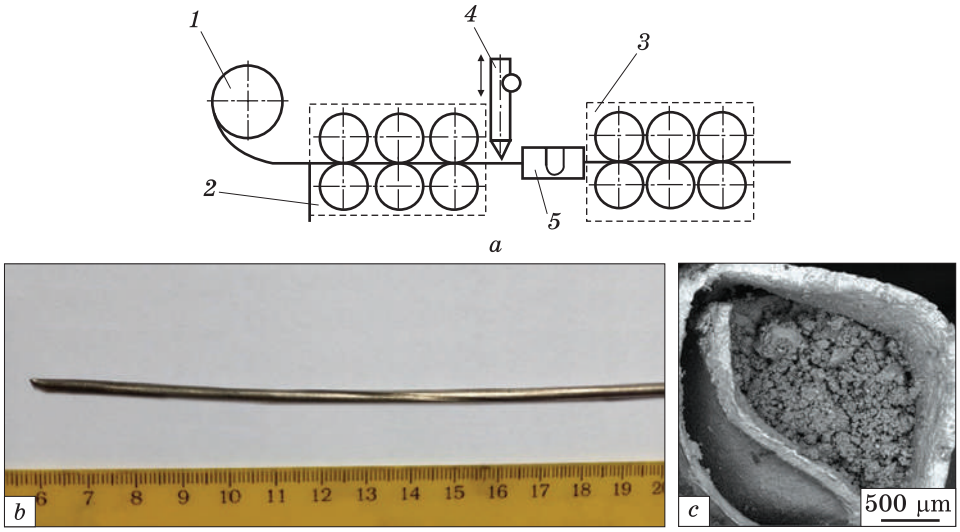

Fig. 3. Manufacturing of Ti–6Al–4V–40%TiC MMC cored wire: (*a*) the general scheme of manufacturing device (*1* — charger; *2* and *3* — rollers; *4* — powder dispenser; *5* — spinner); (*b*) the view of wire produced and (*c*) wire cross section showing foil shell with powder blend inside

why, there is an important task to develop methods to produce wires of corresponding MMC compositions, which can be used as feedstock material for further 3*D* processing and manufacturing of MMC products. The aim of present investigation was development of processing route to produce wire of prescribed MMC composition, further testing of that MMC wire in 3*D* printing process to obtain MMC structures, determination of general rules of microstructure formation and properties of 3*D* printed composites.

3. Manufacturing of Cored Wire

In the present study, the approach to produce wire whose composition corresponds to MMC on the base of Ti–6Al–4V (wt.%) alloy matrix reinforced with 40% (vol.) TiC was developed first. Then, the noted wire was tested in 3*D* printing process to establish the general laws of microstructure formation and properties of MMC products. To produce the wire of Ti–6Al–4V–40%TiC composition, specific technology was developed at E.O. Paton Electric Welding Institute [32–35]. Powder blend of Ti powder (less than 100 μm in size), 60Al–40V (wt.%) master alloy powder (less than 63 μm), and titanium carbide TiC (less than 30 μm) was sealed in titanium foil shell (commercial purity Ti Grade 1, 0.2 mm thickness). The reciprocal amount of the titanium foil shell and powder blend inside was calculated to meet totally the prescribed Ti–6Al–4V–

40% TiC MMC composition. Titanium foil shell was stretched and deformed using special device (Fig. 3, *a*) at simultaneous filling of shell with powder blend to obtain a straight 'wire' 3 mm in diameter (Fig. 3, *b*) and 62% filling of inner space (Fig. 3, *c*). The stretching of foil shell was performed at speed of 30–35 m per hour; set of spinners was used to reduce cross-section of wire on deformation (0.1 mm for each reduction step). Subsequently, the wire was used as feedstock material in xBeam 3*D* printing process using electron beam melting [22–27]. Ti–6Al–4V–40% TiC MMC samples having 10–20 mm horizontal size and up to 12 mm in height were layer-by-layer printed at Ti–6Al–4V cast and wrought substrate to study the general laws of microstructure formation and material characteristics obtained with 3*D* printing process.

The microstructure of the 3*D* printed material was studied using Olympus IX-70 light microscope and a VEGA 3 TESCAN scanning electron microscope (SEM) equipped with Brucker EDX analyzer for investigation of local chemical composition. Local crystallographic orientations (texture) of phase constituents were studied with electron back scattering diffraction (EBSD) method at MIRA 3 TESCAN device. Vickers hardness of 3*D* printed products was measured with a Wolpert Wilson Instruments 452 SVD hardness tester.

4. Reaction Processes between Ti-Matrix Melt and TiC Particles

4.1. General Behaviour of TiC Particles and Diffusion of Carbon under Conditions of Short-Term Melting of the Metal Matrix

Taking into consideration that TiC phase has the melting point (3066 °C [36]) significantly higher than those for titanium (1668 °C) and Ti–6Al–4V alloy, the first step for investigation of 3*D* printing process of MMC was to determine the general behaviour of solid TiC particles inside molten Ti-based pool, including possible wetting of TiC particles with melt. To study the melting and wetting processes, the TiC powder was pressed in a mould at a pressure of 300 MPa to obtain disk sample 30 mm in diameter. Then, the sample was hot pressed in an SPD-120 apparatus [37] using graphite die pre-coated with boron nitride powder to protect the sample from direct interaction with the tools. An induction heating with heat rate 100 °C/min was set to achieve temperature of 2000 °C. The

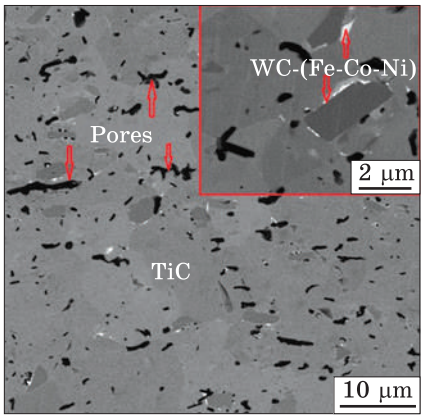

Fig. 4. Microstructure of hot pressed TiC. SEM, BSE

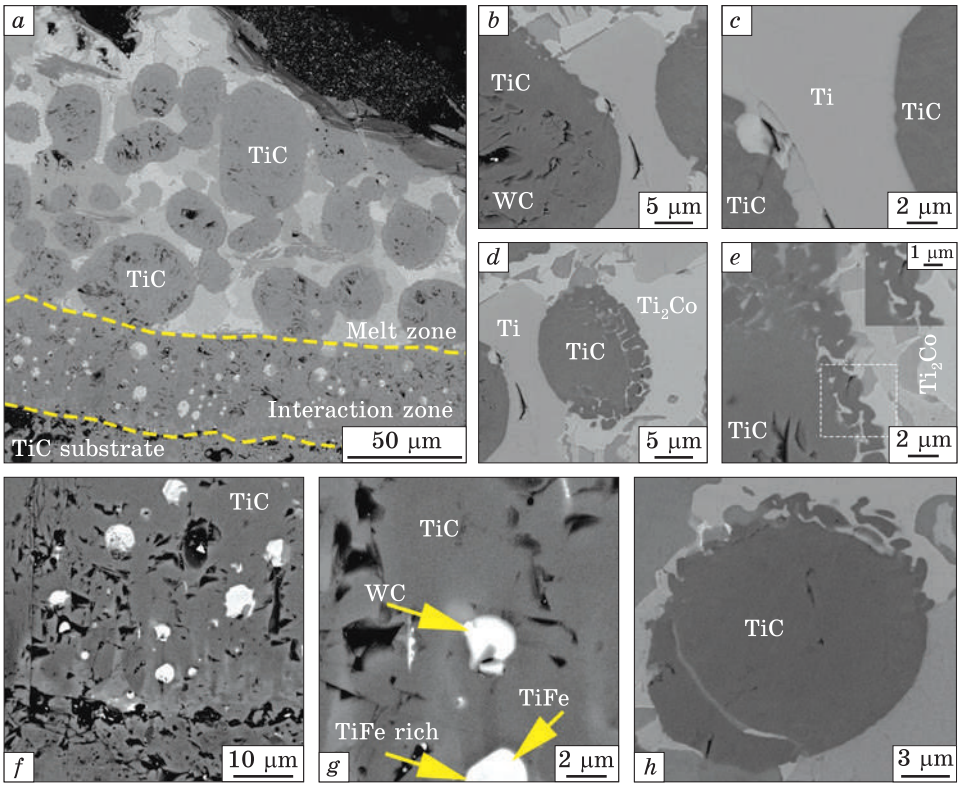

Fig. 5. Cross section of model Ti–TiC system after wetting experiment: (*a*) general view of zones formed at liquid/solid interface, (*b*, *c*) TiC–Ti–TiC interfaces, (*d*, *h*) TiC particles within Ti–Co–Fe–Ni areas, (*e*) small particles of TiC at TiC/Ti–Co–Fe–Ni interface; (*f*) general view of interaction zone, (*g*) microstructure features of interaction zone. SEM, BSE

initial load was 8 MPa and, once achieved the peak temperature, the load was increased to 32 MPa. The dwell time at the maximum temperature was 20 min; the furnace was slowly cooled down to 1200 °C to avoid crack formation. Hot pressed TiC sample was used in wetting experiments, which were carried out by the sessile drop technique [38] in a vacuum furnace.

A small piece of pure Ti was put on the polished surface of the hot pressed TiC substrate, and then the metal/ceramic couple was introduced into the furnace chamber. The chamber was pumped down to a vacuum of 10^{-3} Pa at room temperature and then heated (rate of 50 °C/min) up to the temperature above titanium melting point. The temperature was measured by pyrometer and was 1700 °C. The final contact angles between molten phase and solid TiC were measured after cooling using the ImageJ software [39].

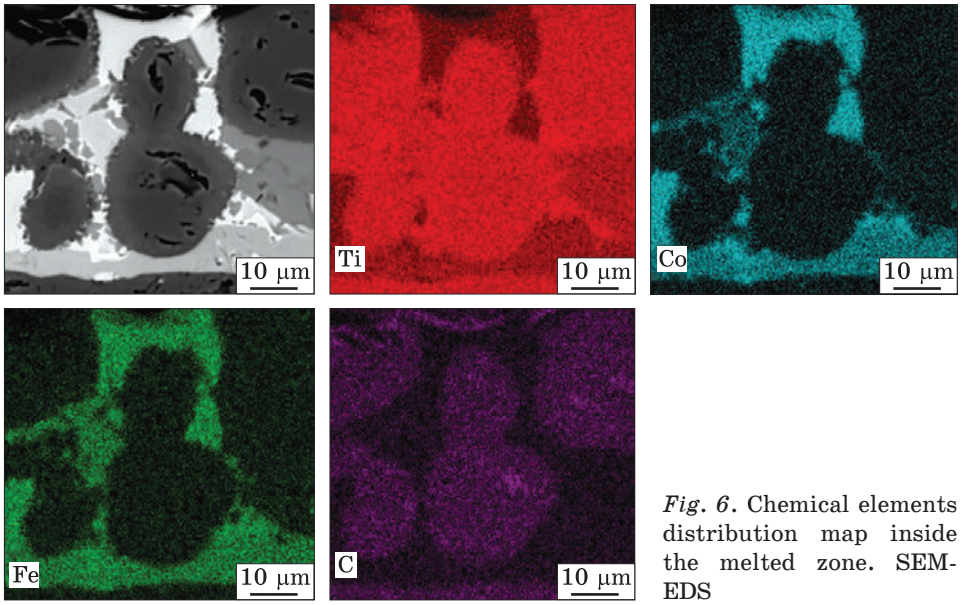

Fig. 6. Chemical elements distribution map inside the melted zone. SEM-EDS

Microstructure of hot pressed titanium carbide sample is shown in the Fig. 4 and is characterized by TiC matrix with complex WC–(Fe–Co–Ni) compound inclusions and 7% residual pores. WC–(Fe–Co–Ni) impurities are a result of TiC powder preparation by milling using tungsten carbide balls, which, in turn, were sintered with Fe–Co–Ni binder. Results of the heating of Ti/TiC couple above titanium melting point can be illustrated with Fig. 5, where cross section of interaction zone between Ti melt (top) and TiC (bottom in Fig. 5, *a*) is shown. In general, microstructure obtained after this experiment contains 3 different zones: 1) melt zone, 2) interaction zone, and zone of TiC substrate (Fig. 5, *a*).

Zone of the melt has a heterophase structure and consists of Ti, Ti_2Co, and TiC components (Figs. 5, *a*–*e*), thus, different elements are not uniformly distributed over the melted zone (Fig. 6). The Ti_2Co phase was formed because of the chemical interaction of Ti melt with WC–(Fe–Co–Ni) compound. The mechanism of Ti_2Co intermetallic formation can be described as a following. On heating up to temperature of about 1550 °C (*i.e.*, quite below titanium melting point) melting of the metallic binding in the WC–(Fe–Ni–Co) hard compound occurs. The Fe–Ni–Co liquid phase (in which cobalt predominates) interacts with solid titanium, saturating b-Ti phase with noted b-stabilizing elements with subsequent formation of the Ti_2Co phase and the beginning of the TiC dissolution in Ti–Fe–Ni–Co solution.

According to the phase equilibrium diagrams for Fe–TiC, Co–TiC, and Ni–TiC systems, the solubility of the titanium carbide is within

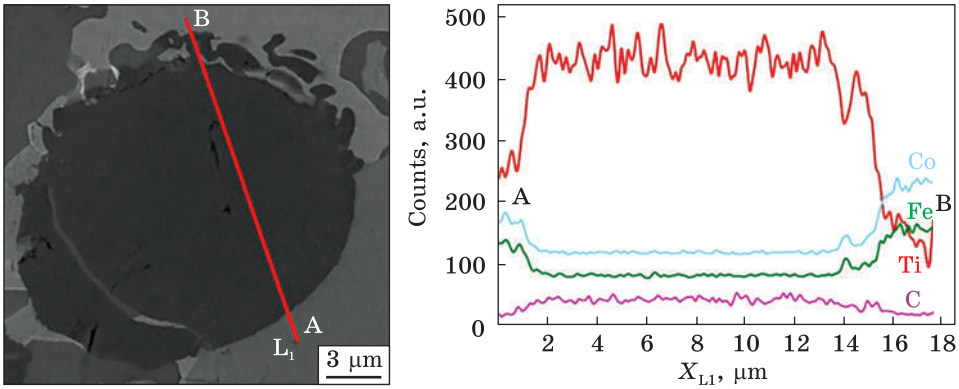

Fig. 7. The distribution of chemical elements around TiC particle along the line L_1. SEM-EDS quantitative analysis

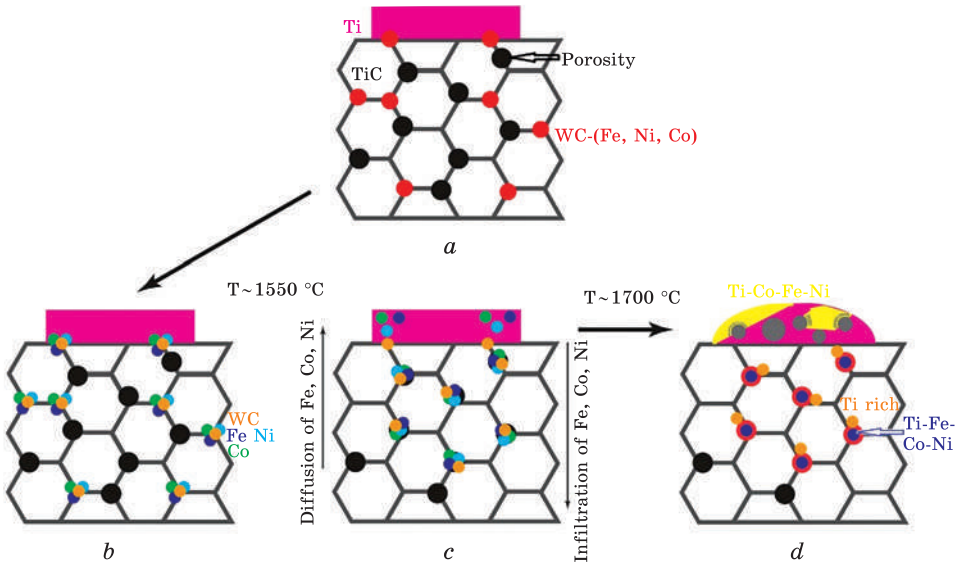

Fig. 8. Scheme of interaction between components in TiC–Ti system during wetting experiment

1.5–6 mol.% [40]. WC did not participate in the interactions and did not form new compounds, its solubility in titanium carbide, titanium, or cobalt does not exceed 2 at.% [40]. When the temperature of the wetting experiment (1700 °C) is reached, titanium completely melts starting a liquid-phase interaction with TiC substrate. The interaction process takes place in the mode of TiC substrate dissolution, as indicated by the shape of titanium carbide particles, Fig. 5, *b–e*. At the interface of Ti–Fe–Ni–Co liquid, small TiC particles with a size of 2–5 μm form due to the classical mechanism of dissolution inherent for the systems

TiC–Fe, TiC–Co, TiC–Ni [41, 42]. Bearing in mind that the initial TiC powder (before sintering) had particles of similar sizes, it can be assumed that, when interacting with the metal melt, titanium carbide 'remind' its primary structure, obviously due to the peculiarities of the bonding between sintered particles. Contrary, part of TiC contacting with pure titanium melt has a sharp boundary (Fig. 5, *d*) that indicates a rather weak interaction between TiC and molten Ti. The distribution of elements throughout the TiC particle and across two boundaries along its edges (Fig. 7) indicates the preservation of a relatively sharp boundary between Ti melt and TiC (point *A*), while the boundary between Ti–Fe–Ni–Co melt and TiC (point *B*) is blurred due to more active mutual interaction with the formation of small TiC particles. In general, due to diffusion activation, the TiC phase does not maintain its stoichiometry during heating to noted temperatures.

In the interaction zone, the phase composition is represented by TiC with Ti–Fe and WC inclusions (Fig. 5, *f*, *g*). The higher amount of impurities Fe (≈23 at.%), Ni (2 at.%) and Co (≈6 at.%) in the Ti–Fe–Co–Ni matrix can be explained below, using the general scheme of interaction between Ti and TiC shown in Fig. 8.

When the Ti–TiC contact pair (Fig. 8, *a*) is heated, the metallic binding compound (Fe–Co–Ni) contained in {WC–(Fe–Co–Ni)} impurity melts at a temperature of about 1550 °C (Fig. 8, *b*). The liquid Fe–Co–Ni phase appeared at the grain boundaries inside the sintered TiC compact below the contact surface with titanium. Then, liquid redistributed between the TiC grains and fill the residual pores, which is confirmed by the formation of separate WC inclusions (Fig. 5, *g*) in which there is no metallic bond. A similar extraction of bindings from a WC-based hard alloy and other carbides was observed [42]. At the same time, the Fe–Co–Ni liquid that is in contact with pure titanium is spent acting with it (Fig. 8, *c*). The interaction process is characterized by the formation of the b-Ti phase in the initial stages, while the subsequent increase in temperature to 1700 °C leads to the formation of a titanium-based liquid enriched in Fe–Co–Ni (Fig. 8, *d*). Simultaneously, molten titanium penetrates inside sintered TiC compact and interacts with the Fe–Co–Ni liquid.

As a general result of wetting experiment, sufficiently high wetting of solid TiC particles with molten phases was established from the analysis of the final contact angles between phases after material cooling. Liquid phase of pure titanium wets TiC surface with contact angle of 50° without formation of any intermediate phases. Having the lowest contact angle (≈14°), the Fe-enriched melt redistributed between TiC grains and filled the pores, forming a dense zone. At the same time, Ni and Co remained in the zone of the molten metal have the wetting angles 20° and 30°, respectively [43, 38].

At a temperature of 1700 °C, all metal elements are in the liquid phase. According to the Ti–Co binary phase diagram, formation of two liquid phases (pure Ti and Ti_2Co) is thermodynamically favourable in liquid area. The mechanisms of interaction of liquid Ti with TiC and liquid Ti_2Co with TiC are different. In the first case, the boundary is clean without a change in the chemical composition along the cross-section of the b-grain, and TiC dissolution is weakly expressed. In the second case, the process of TiC dissolution is more pronounced, because the amount of dissolved TiC in Co is greater than in pure titanium. Below the molten titanium drop (Fig. 8, *d*), the interaction occurs due to the redistribution of Fe–Co–Ni elements. Molten titanium penetrates the areas enriched in Fe–Co–Ni and forms a core–shell (gradient) structure of inclusions, Fig. 5, *g*, the shell of which is the Fe_2Ti phase, and the core is the TiFe phase. The formation of such a gradient structure was also revealed when studying the interaction between Fe and Ti [44].

Therefore, pure titanium melt is reacting with titanium carbide less actively, as compared with the presence of Fe, Ni, or Co impurities, which changes the interaction process and leads to the formation of small TiC crystals because of the massive TiC matrix dissolution.

4.2. Possible Redistribution of TiC Particles n the Ti-Based Melt because of Thermogravitational Convection

Since the Ti–6Al–4V matrix alloy and titanium carbide differ somewhat in density (4.43 g/cm^3 for the alloy *versus* 4.9 g/cm^3 for TiC), we considered it necessary to check the probability of displacement of heavier TiC particles towards the bottom part of the MMC volume because of the alloy matrix melting. At the same time, ascending convection flows should exist in the molten alloy, which, on the contrary, in theory can move TiC particles towards the top of the melt. To test the possible effect of these two mutually opposite factors, an additional experiment was carried out: MMC Ti–6Al–4V + 40% TiC preliminary produced with powder technology (press-and-sintered) was remelted in a laboratory vacuum-arc furnace [45]. The sample for such experiment had a weight of 40 g and a small size in order to be as close as possible to the melting conditions for 3*D* printing of MMC with powder wire. Microstructure of remelted MMC is presented in Fig. 9.

As can be seen from Fig. 9, microstructure of remelted MMC is rather uniform from point of view of amount of TiC particles in all locations including top (Fig. 9, *a*), centre (Fig. 9, *b*), and bottom (Fig. 9, *c*) parts of the ingot, excepting very thin rim on the bottom edge that could be related to extreme cooling conditions on water-cooled copper hearth of the furnace. This means that both above mentioned possible processes (convection floating up or sinking to the bottom of the heavi-

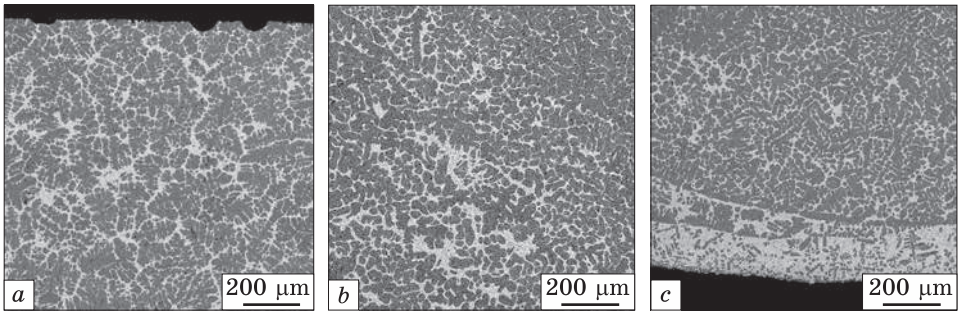

Fig. 9. Microstructure of Ti–6Al–4V + 40% TiC MMC remelted in vacuum arc furnace: (*a*) top, (*b*) centre, and (*c*) bottom of the ingot

er TiC component) mutually did not have obvious effect. Perhaps the latter process is even absent due to the fact of active diffusion of carbon from TiC particles into the titanium matrix, because of which the specific gravity of the metal matrix and inclusions converge even more. It can be noted some difference in the morphology of TiC crystals in the top and bottom parts of the ingot (Fig. 9, *a vs.* 9, *c*). In the upper part of the ingot, almost all titanium carbides have a manifested dendritic morphology (Fig. 9, *a*), while in the centre (Fig. 9, *b*) and especially in the bottom part (Fig. 9, *c*), at least some of them retain their shape close to equiaxed, which was in the initial sintered MMC (Fig. 1, *b*). Such a difference in the microstructure can be explained by some variation in temperature along the height of the melt, *i.e.*, in the upper part, where there was a direct impact of the arc, the temperature was higher than in the lower part, where heat was removed towards the water-cooled copper hearth.

5. Microstructures Formed on 3*D* Printing

The experiments on 3*D* printing of Ti–6Al–4V–40% TiC MMC with cored wire were started from production of single (*A*, Fig. 10), and few-layers (*B* in Fig. 10) samples.

Microstructure of printed MMC layers and heat affected zone within the Ti–6Al–4V plate used as a substrate was studied in the vertical cross sections cut through the middle of the printed beans and along printing direction (as it is shown in Fig. 10).

The ability to simultaneously melt both the wire feedstock and the substrate around the feed point (*i.e.*, to create a melt pool) with the profiled electron beam is one of the essential advantages of the xBeam process. But, when using a cored wire, this technique did not work properly: part of the electron beam that fell directly on the wire instantly melted the thin (<0.2 mm) shell of the cored wire and released the powder, which immediately flew in all directions due to electro-

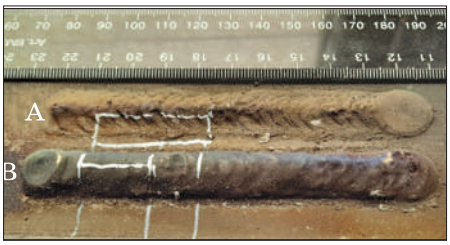

Fig. 10. General view of 3*D* printed single (*A*) and several (*B*) MMC layers on the Ti–6Al–4V base plate

Fig. 11. xBeam process configuration with melting the cored wire feedstock by energy accumulated in the melt pool

static repulsion caused by the picking up electrons by free powder particles. Due to this, only a tiny part of the powder entered the melt pool, leading to significant deviations from the settled chemical composition. In addition, the scattered powder partially fell into the discharge chamber of the electron gun and onto the cathode causing breakdowns that significantly worsened the stability of the deposition process, resulting in a further declined the uniformity of the distribution of MMC components in the 3*D* printed material.

To prevent these phenomena, the configuration of the mutual placement of the process elements (the profile electron beam, the wire, and the substrate) was adjusted in such a way that the electron beam did not fall directly on the wire and, accordingly, did not melt it above the substrate. For this, the substrate was placed closer to the gun. In this configuration, all electron beam energy fell on the substrate, creating a wider and deeper melt pool than usually done using a conventional wire. In this way, the cored wire was immersed in the melt pool and melted there due to the energy accumulated in the pool, keeping the sheath in a solid state above the pool during the entire deposition process (Fig. 11). Due to this, the sheath prevented the powder from being released before it entered the liquid metal in the pool. This solution made it possible to ensure a reasonably stable deposition process and relatively uniform distribution of MMC components throughout the volume of the 3*D* printed sample. True, such a solution became possible under the condition of excessive heat investment in the substrate. However, the effect of such overheating on the structure still needs to be studied.

Above noted problems were the reasons of not optimized structure of 3*D* printed MMC products (Fig. 12) obtained during first testing experiments using cored wire. In addition to pores (some of them were up to 500–600 microns in size (Fig. 12, *a*)), visible inhomogeneity of matrix microstructure and titanium carbide precipitations of various morphology not uniformly distributed over the alloy matrix (Figs. 12, *b*–*f*) were observed as distinctive features of printed MMC products. In the

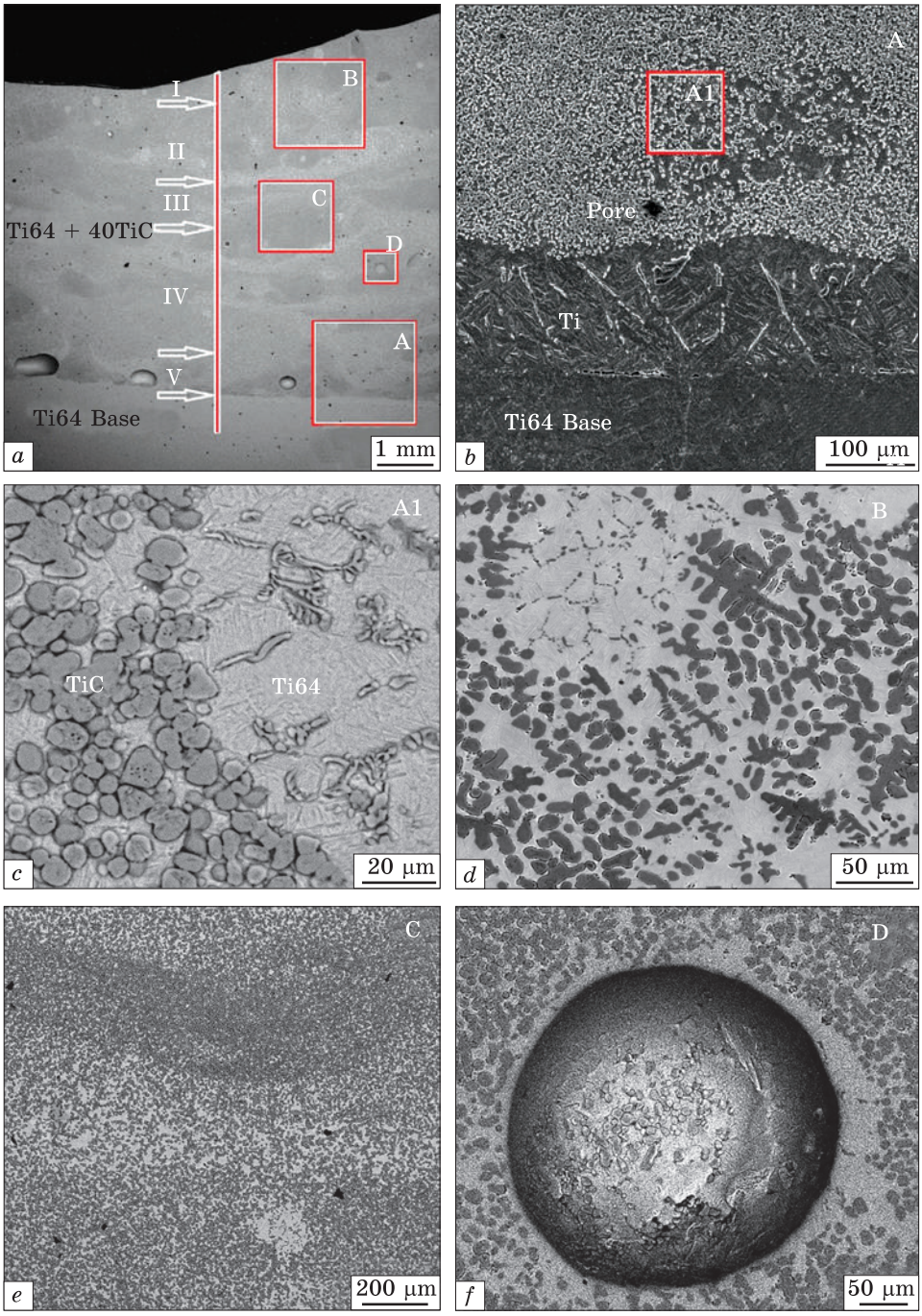

Fig. 12. Typical SEM images of 3*D* printed products obtained in testing experiments. (*a*) General view of Ti–6Al–4V–40% TiC MMC at Ti–6Al–4V base plate with indicated line where hardness was measured and locations of detailed microstructural analysis: (*b*) zone (*A*) inside non-uniform layer of low-alloyed titanium between base substrate and MMC; (*c*) zone (*A*1) with non-uniform distribution of TiC, (*d*) dendritic type of TiC inside zone (*B*), (*e*) zone (*C*), and (*f*) pore inside zone (*D*) with fine TiC particles on its inner surface and around. SEM, BSE

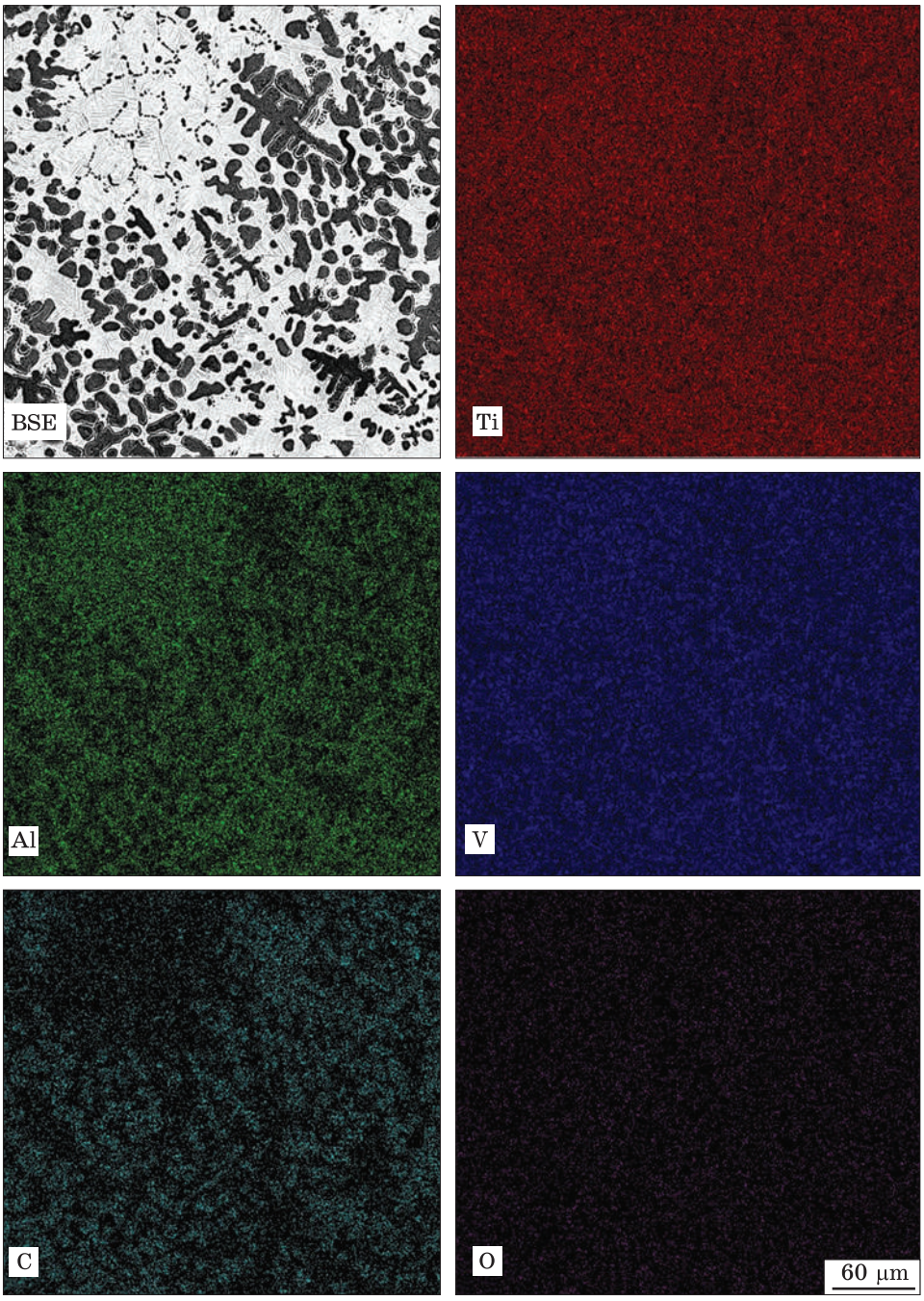

Fig. 13. SEM BSE image, and maps of elements distribution inside the zone (*B*) (shown in Fig. 12, *d*)

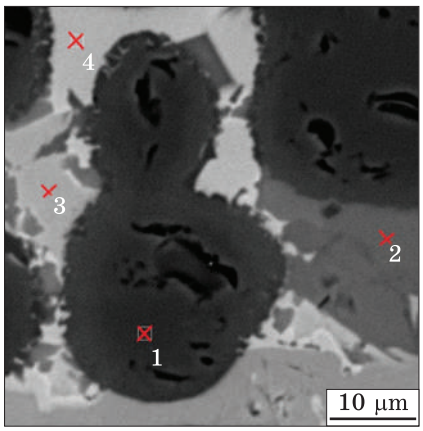

Fig. 14. Not smooth edges of TiC particles and points of local chemical composition analysis showing different Carbon content within surrounding remelted matrix. SEM, BSE

best case, when the entire cored wire material enters the melting zone uniformly, its melting and crystallization led to formation of lamellar *a* + + *b* alloy matrix, whose composition was close to prescribed Ti–6Al–4V alloy material with rather homogeneously distributed crystals of TiC. At the same time, areas having an obvious deficit of alloying elements (Al and V) and a deficit of carbide particles were observed in the matrix, for instance, in the layer adjusting to the Ti–6A–4V baseplate (zone (*A*) in the Fig. 12, *a*, also shown at higher magnification in Fig. 12, *b*). Probably, such areas are the result of a non-uniform supply of the powder blend to the melting zone, when the melted material was enriched with titanium due to the foil used for the wire shell. As was shown by EDX, local chemical composition of such matrix areas was close to unalloyed titanium (96% Ti, 3% C, 1% Al) that confirms above assumption. As for the layers located above (zone (*A*1) in Figs. 12, *b* and *c*), both a lamellar a + b matrix and dispersed TiC particles (nearby globular one 5–10 μm in size that is rather close to initial size of used powder [16]) are observed (Fig. 12, *c*). However, the crystals of the hardening phase are not very uniformly distributed, which is also most likely caused by the uneven supply of the powder components of the wire.

In the upper part of the 3*D* printed material, where the melt temperature was obviously the highest, the formation of TiC crystals in the form of dendrites was found (Fig. 12, *d*). Study of chemical composition in this zone showed that the distribution of carbon is most inhomogeneous in comparison with all others elements (Fig. 13). In the central part of the printed material, the 'layered' microstructure was observed in terms of the density and uniformity of the distribution of dispersed TiC particles (area *C* in Fig. 12, *a* and its magnified image in Fig. 12, *e*).

The structural features of the internal surfaces of the pores should also be mentioned. First of all, the surface of the pore is characterized by a sufficiently high smoothness, and its structure actually repeats the microstructure of the surrounding MMC material, namely, similar dispersed particles and individual sections of the titanium lamellar a + b matrix (Fig. 12, *f*).

Apart from purely thermal considerations, the formation of dendritic type of titanium carbide precipitations can be explained from the analysis of Ti–C binary phase diagram. Carbon content in starting TiC powder observed with EDX analysis was within 25–51 at.% in various particles at average carbon content of 47%. It is seen from Ti–C binary phase diagram [36], the formation of liquid phase is possible at 1645 °C if carbon content is below 30%, and noted temperature is a little lower than titanium melting point (1668 °C). Taking into consideration relatively fast diffusion mobility of C in titanium [1], and active diffusion of carbon from TiC particles to surrounding Ti-based matrix at high temperatures [46], which led to reduction of carbon content in carbides below stoichiometric TiC composition (50 at.% Ti and C), partial melting of initial TiC particles can be assumed on 3*D* printing process together with melting of Ti foil and Ti powder. Further solidification of such Ti–C system results in formation of dendritic morphology of titanium carbide precipitations.

To confirm the carbon redistribution related to partial melting and dissolution of TiC particles, local composition in detail was studied in the sample described in Sec. 4.1. In this experiment, a piece of titanium was melted on the surface of a massive hot pressed TiC sample. The area presented in Fig. 6 was examined, but local chemical compositions were measured inside 4 different locations indicated in Fig. 14. Results of EDX analysis are listed in Table 1. After Ti melting, titanium carbide particles with dissolved edges are surrounded by titanium matrix saturated with Fe, Co, Ni impurities (Table 1) inevitably presented in TiC powder as a result of powder manufacturing process. In addition to 'toothed' edges of titanium carbide particles, partial dissolution of carbides during short-time melting process was accompanied with reduction of carbon content inside them (Table 1) as well as saturation of surrounding titanium matrix with carbon. As seen in Fig. 14, and points 3, 4 in Table 1, dissolution of TiC particles is more pronounced at the edges enriched with the Fe and Co impurities that obviously promotes melting.

Table 1. **Local chemical composition of carbide particles and surrounding titanium matrix (Fig. 14) after melting**

Point in Fig. 14	Content of elements (at.%)				
	Ti	C	Fe	Co	Ni
1	81.4	18.5	<0.1	<0.1	<0.1
2	96.0	3.4	0.2	0.3	0.1
3	84.5	5.9	5.7	3.6	0.3
4	65.6	6.2	8.7	14.9	4.6

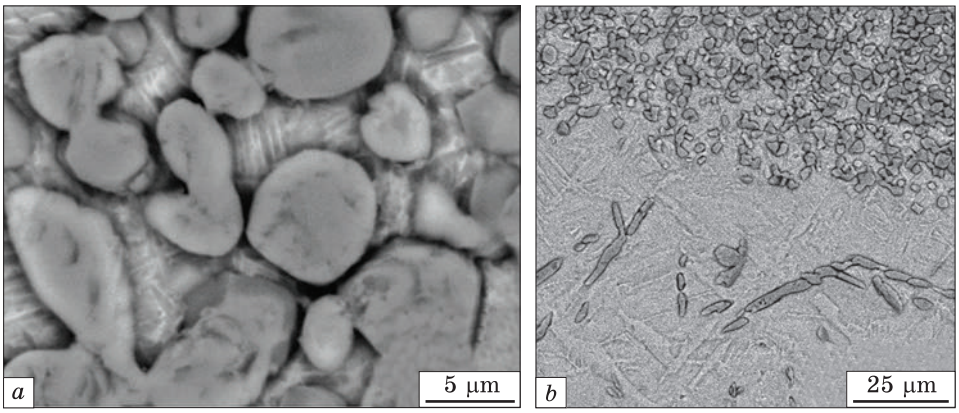

Fig. 15. Formation of densely spaced carbide chains (*a*) and distantly separated titanium carbide precipitations (*b*) in alloyed titanium matrix. SEM, BSE

Melting point of 60% Al–40% V master alloy (1405 °C [47]) is even lower than those are for other constituents of the wire (Ti foil, Ti and TiC powders). Therefore, Ti–Al–V–C molten pool (with presence of Fe, Co and Ni impurities) and solid remnants of initial TiC particles inside are formed in heating area on 3*D* printing process. Titanium carbides of various morphologies (Figs. 15), including chains of bonded particles and elements of dendritic structure were observed on subsequent crystallization. Local carbon content within 21–30 at.%, *i.e.*, noticeably lower than that for stoichiometric TiC composition, was determined in densely spaced neighbouring carbide precipitations (like those shown in Fig. 15, *a*), while distantly separate particles (Fig. 15, *b*) in alloy matrix were the most depleted with carbon (21% at. C).

Above data presented in chapters 4.1 and 4.2 demonstrated that during conventional melting process, TiC particles rather uniformly distributed over the titanium-based molten pool due to sufficient surface wetting ability of TiC particles with the melt, their comparable densities and/or intensive mixing of molten material. Investigation with EBSD method of similar relatively uniform MMC areas obtained with 3*D* printing approach (Fig. 16) also confirmed formation of rather isotropic structure of Ti–6Al–4V alloy matrix with fine (5–10 μm) a phase (Fig. 16, *b*), β phase (Fig. 16, *c*), and TiC (Fig. 16, *d*) crystallites. No obvious crystal texture of all phase constituents (a and b ones for Ti–Al–V matrix as well as TiC phases) was not determined for 3*D* printed material from EBSD observations. At first glance, this result looks somewhat unexpected, taking into account the fact that in the case of 3*D* printing by the same method of the Ti–6Al–4V alloy, a rather sharpened crystallographic texture takes place, caused by strictly directed heat flow during wire melting and subsequent crystallization of the

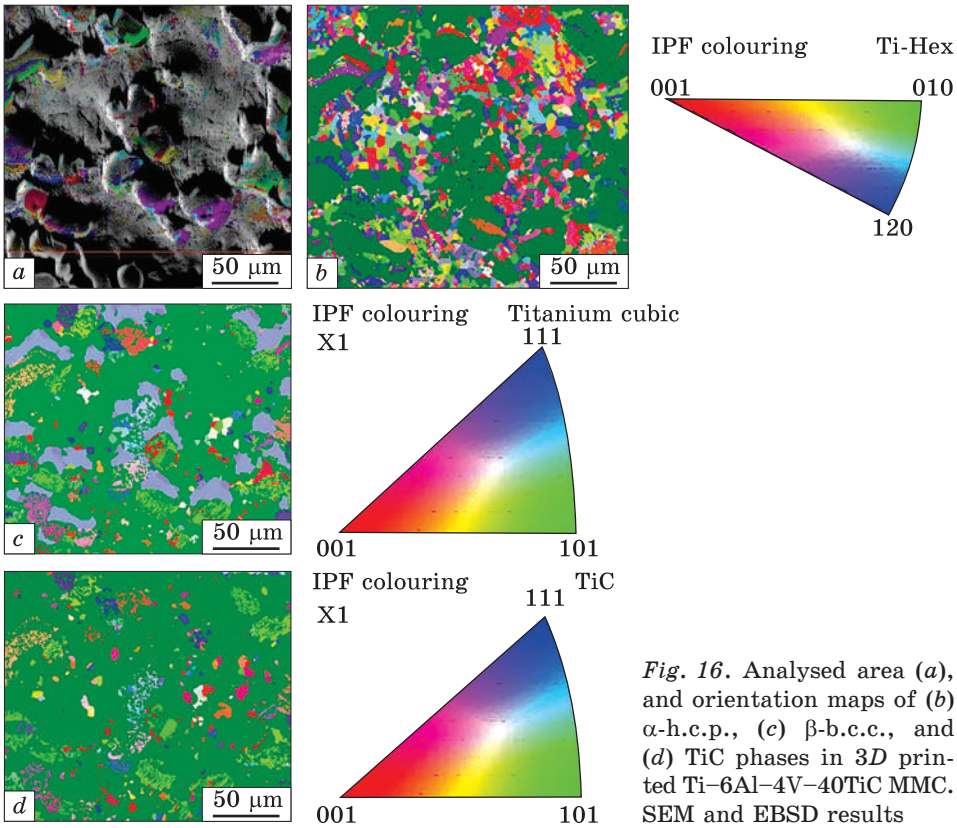

Fig. 16. Analysed area (*a*), and orientation maps of (*b*) α-h.c.p., (*c*) β-b.c.c., and (*d*) TiC phases in 3*D* printed Ti–6Al–4V–40TiC MMC. SEM and EBSD results

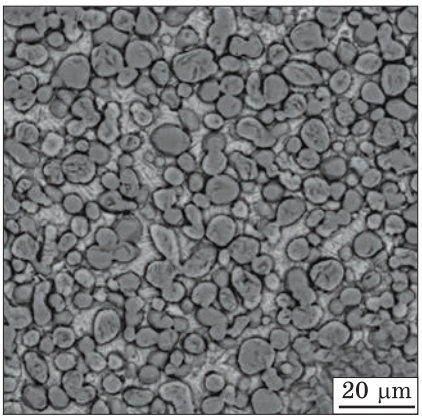

Fig. 17. Improved microstructure of 3*D* printed material after optimization of processing parameters. SEM, BSE

melt [24–26]. In our opinion, in MMC case, the crystallographic randomness of the orientation of crystallites of the a and b phases is determined by the fact that, during cooling, the high-temperature b phase crystallizes on still solid (or crystallized first) TiC particles. TiC particles, by their nature, have a random orientation, given by the processes of grinding and mixing, thus promoting random orientation of b titanium crystals nucleating on their surface. In the process of further cooling, the high-temperature b phase releases a certain amount of the a phase, which crystallography is specified by 12 Burgers orientation relationships [1, 48].

Summarizing all above, it is possible to conclude that microstructure inhomogeneity observed in printed MMC (Figs. 12, *b–e*) can be related to not uniform powder distribution inside the wire and not steady feed of wire to a heating/melting area.

Further adjustment of 3*D* printing regimes with change the process configuration to melt the cored wire feedstock by energy accumulated in the melt pool (Fig. 11) allowed manufacturing of relatively homogeneous Ti–6Al–4V alloy matrix with rather uniform distribution of mainly globular TiC particles inside (Fig. 17). Some occasional pores can be found in 3*D* printed products, despite of the number and size of pores was noticeably reduced.

6. Hardness

To evaluate mechanical characteristics of 3*D* printed MMC material and its uniformity over the height of the printed zone, Vickers hardness was determined as dependence of layer depth (Fig. 12, *a*). As presented in Fig. 18, *a*, in case of not optimized first attempts of 3*D* printing, 6 separate locations (zones), which have essential difference in hardness, can be identified. Top surface zone *I* is slightly depleted by TiC particles (top of Fig. 12, *a*), and alloying elements due to relatively long exposure of this upper layer in melted state, that caused a little lower level of hardness (around 400 *HV*). Next zone (*II*) represented by TiC of dendrite morphology (Fig. 12, *d*), in which hardness is varied between 480

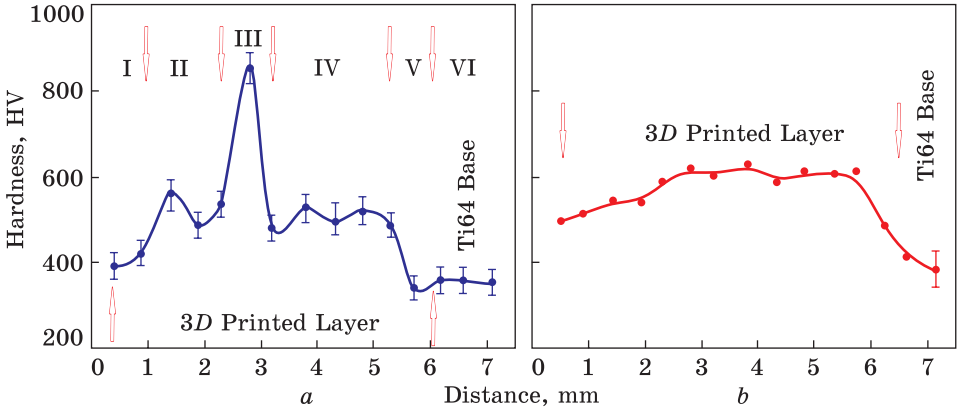

Fig. 18. Hardness distribution *vs*. distance from the surface of MMC 3*D* printed with several passes after (*a*) primary experiments, and (*b*) adjusted 3*D* process. Zones in (*a*): *I* — surface with reduced amount of TiC (Fig. 12, *a*), *II* — top layer with dendrite morphology of TiC (Fig. 12, *d*), *III* — area with high density of fine equiaxed TiC (Fig. 12, *e*), *IV* — area with not uniform distribution of TiC (Fig. 12, *c*), *V* — area depleted by TiC and alloying elements (Fig. 12, *a*, layer adjacent to the Ti–6–4 based plate), *VI* — Ti–6Al–4V based plate

and 577 *HV* depending on size and spatial density distribution of carbide crystals. Zone *III* is characterized by the highest hardness above 800 *HV* that is a result of high and uniform spatial density of fine equiaxed TiC particles (Fig. 12, *e*). Within the widest zone *IV*, hardness again varied within a similar range 470–560 *HV* that is a result of described above non-uniformity in TiC distribution (Fig. 12, *c*). Thin layer near the boundary with Ti–6Al–4V plate (zone *V*) has the lowest hardness, because it is a layer of titanium containing a small amount of alloying elements, and moreover, obvious deficit of hardening TiC particles (Fig. 12, *b*). The base Ti–6Al–4V plate is characterized by hardness level of about 340 ± 15 *HV* usual for commercial cast and wrought alloy.

In the case of obtaining a more uniform MMC microstructure (like that shown in Fig. 17) after adjustment of the 3*D* printing regimes, the dependence of hardness on distance from the sample surface has a somewhat smoother character (Fig. 18, *b*), and fluctuates within a relatively narrow range of 490–615 *HV* inside the printed MMC layer, smoothly descending to 360 *HV* for the Ti–6Al–4V base layer.

Usually, 3*D* printed materials require achievement of uniform microstructure and mechanical characteristics. Material with optimized microstructure (Fig. 17) and relatively uniform hardness over a 3*D* printed layer (Fig. 18, *b*) looks very promising for successful application of used technology employing cored wire as feedstock material for production of titanium-based MMCs of various composition. However, laminated materials which combine layers of different chemical compositions and microstructures with corresponding gradient of characteristics (like that shown in Fig. 18, *a*, for hardness) are rather interesting for alternative applications where layered materials may have advantages in mechanical and service properties [49]. Employment of described 3*D* printing approach for manufacturing of layered structures which combine MMC and alloy layers and example of promising application of combined MMC/alloy materials will be presented in our next study (see Part 2 [50]).

7. Conclusions

• Cored wire consisted of titanium foil shell and powder blend corresponding to the MMC composition of Ti–6Al–4V and 40 vol.% TiC was produced and used in xBeam 3*D* printing technology for manufacturing of Ti–6Al–4V–40% TiC MMC layer on the base of commercial Ti–6Al–4V plate.

• The general rules of MMC microstructure formation on melting and crystallization cycle on 3*D* printing were established. Sufficient wetting of solid TiC particles and their partial dissolution in surrounding Ti-based melt with carbon redistribution between solid TiC rem-

nants and alloyed liquid phase, on further cooling results in formation of lamellar $\alpha + \beta$ matrix with titanium carbide precipitations of various morphologies inside.

• Adjustment of 3*D* printing regimes allowed formation of isotropic MMC structure with relatively uniform distribution of titanium carbide precipitations having mainly equiaxed morphology inside Ti–6Al–4V alloy matrix.

• 3*D* printed Ti–6Al–4V–40% TiC MMC was characterized with hardness of 490–615 *HV*; such values are markedly higher than those are for Ti–Al–4V alloy, suggesting the manufacturing approach is promising for wide industrial application.

Acknowledgements. The work was carried out without special funding. However, separate structural studies were performed within the project 'New Metal-Containing Materials and Innovation Technologies for Priority Branches of Ukrainian Industry' (State Reg. No. 0123U100898) under the budget program КПКВК 6541230 of the National Academy of Sciences of Ukraine.

REFERENCES

1. U. Zwicker, *Titan und Titanlegierungen* (Berlin: Springer-Verlag: 1974).
2. G. Luetjering and J.C. Williams, *Titanium. 2nd Ed.* (Berlin: Springer: 2007); https://doi.org/10.1007/978-3-540-73036-1
3. R.I. Jaffee and H.M. Burte, *Titanium Science and Technology* (Berlin: Springer: 1973); https://doi.org/10.1007/978-1-4757-1346-6
4. D. Miracle, *Compos. Sci. Technol.*, **65**, Nos. 15–16: 2526–2540 (2005); https://doi.org/10.1016/j.compscitech.2005.05.027
5. Z.X. Du, S.L. Xiao, P.X. Wang, L.J. Xu, Y.Y. Chen, and H.K.S. Rahoma, *Mater. Sci. Eng. A*, **596**, No. 71: 2526–2540 (2014); https://doi.org/10.1016/j.msea.2013.12.043
6. M. Eriksson, D. Salamon, M. Nygren, and Z. Shen, *Mater. Sci. Eng. A*, **475**, Nos. 1–2: 101–104 (2008). https://doi.org/10.1016/j.msea.2007.01.161
7. P. Wanjara, R.A.L. Drew, J. Root, and S. Yue, *Acta Mater.*, **48**, No. 7: 1443–1450 (2000); https://doi.org/10.1016/s1359-6454(99)00453-x
8. K.B. Panda and K.S. Ravi Chandran, *Metall. Mater. Trans. A* **34**, No. 9: 1993–2003 (2003); https://doi.org/10.1007/s11661-003-0164-3
9. D. Zhu, L. Zhang, W. Wu, L. Lu, J. Song, X. Ni, W. Zhu, J. Zhao, S. Gu, and X. Shan, *J. Phys.*, **1838**, No. 1: 012039 (2021); https://doi.org/10.1088/1742-6596/1838/1/012039
10. O.M. Ivasishin and V.S. Moxson, *Low-Cost Titanium Hydride Powder Metallurgy, Titanium Powder Metallurgy: Past, Present and Future* (New York: Elsevier: 2015), p. 117–148; https://doi.org/10.1016/B978-0-12-800054-0.00008-3
11. O.M. Ivasishin, V.M. Anokhin, A.N. Demidik, and D.G. Savvakin, *Key Eng. Mater.*, **188**: 55–62 (2000);

https://doi.org/10.4028/www.scientific.net/kem.188.55
12. M. Qian, L. Junjie, and G. Mingyuan, *J. Lake Sci.*, **22**, No. 1: 29–34 (2010); https://doi.org/10.18307/2010.0104
13. O.M. Ivasishin, P.E. Markovsky, D.G. Savvakin, O.O. Stasiuk, M.N. Rad and S.V. Prikhodko, *J. Mater. Process. Technol.*, **269**: 172–181 (2019); https://doi.org/10.1016/j.jmatprotec.2019.02.006
14. P.E. Markovsky, D.G. Savvakin, O.M. Ivasishin, V.I. Bondarchuk, and S.V. Prikhodko, *J. Mater. Eng. Perform.*, **28**, No. 9: 5772–5792 (2019); https://doi.org/10.1007/s11665-019-04263-0
15. S.V. Prikhodko, P.E. Markovsky, D.G. Savvakin, O.O. Stasiuk, M.N. Rad, C. Choi, and O.M. Ivasishin, *Microsc. Microanal.*, **24**, No. S1: 2218–2219 (2018); https://doi.org/10.1017/s1431927618011571
16. P.E. Markovsky, D.G. Savvakin, O.O. Stasyuk, M. Mecklenburg, M. Pozuelo, C. Roberts, V. Ellison, and S.V. Prikhodko, *Mater. & Des.*, **234**: 112208 (2023); https://doi.org/10.1016/j.matdes.2023.112208
17. S. Prikhodko, D. Savvakin, P. Markovsky, O. Stasiuk, N. Enzinger, F. Deley, B. Flipo, A. Shirzadi, H. Davies, P. Davies, J. Penny, K. Bozhilov, and O. Ivasishin, *Microsc. Microanal.*, **25**, No. S2: 812–813 (2019); https://doi.org/10.1017/s1431927619004793
18. S. Liu and Y. C. Shin, *Mater. & Des.*, **164**: 107552 (2019); https://doi.org/10.1016/j.matdes.2018.107552
19. A.H. Chern, P. Nandwana, T. Yuan, M.M. Kirka, R.R. Dehoff, P.K. Liaw, and C.E. Duty, *Int. J. Fatigue*, **119**, 173–184: (2019); https://doi.org/10.1016/j.ijfatigue.2018.09.022
20. T. Nagase, T. Hori, M. Todai, S.-H. Sun, and T. Nakano, *Mater. & Des.*, **173**, 107771: (2019); https://doi.org/10.1016/j.matdes.2019.107771
21. L.E. Murr, *Metallogr. Microstruct. Anal.*, **7**, No. 2: 103–132: (2018); https://doi.org/10.1007/s13632-018-0433-6
22. *Patent of the USA No.10,695,835 B2 'Method and Apparatus for Manufacturing of Three Dimensional Objects'* (June 30, 2020).
23. D. Kovalchuk, V. Melnyk, I. Melnyk, and B. Tugai, *Ehlektrotekhnika & Ehlektronika E+E*, **51**, Nos. 5–6: 37 (2016); https://epluse.ceec.bg/wp-content/uploads/2018/08/20160506-full.pdf
24. D. Kovalchuk and O. Ivasishin, *Profile Electron Beam 3D Metal Printing, Additive Manufacturing for the Aerospace Industry* (Elsevier: 2019), p. 213–233; https://doi.org/10.1016/b978-0-12-814062-8.00012-1
25. D. Kovalchuk, V. Melnyk, I. Melnyk, D. Savvakin, O. Dekhtyar, O. Stasiuk, and P. Markovsky, *J. Mater. Eng. Perform.*, **30**, No. 7: 5307–5322 (2021); https://doi.org/10.1007/s11665-021-05770-9
26. D. Kovalchuk, V. Melnyk, and I. Melnyk, *J. Mater. Eng. Perform.*, **31**: 6069–6082 (2022); https://doi.org/10.1007/s11665-022-06994-z
27. A.E. Davis, J.R. Kennedy, D. Strong, D. Kovalchuk, S. Porter, and P.B. Prangnell, *Materialia*, **20**: 101202 (2021); https://doi.org/10.1016/j.mtla.2021.101202
28. J. Hu, J. Zhang, Y. Wei, H. Chen, Y. Yang, S. Wu, D. Kovalchuk, E. Liang, X. Zhang, H. Wang, and A. Huang, *JOM*, **73**, No. 7: 2241–2249 (2021); https://doi.org/10.1007/s11837-021-04712-z
29. O.M. Ivasishin, D.V. Kovalchuk, P.E. Markovsky, D.G. Savvakin, O.O. Stasiuk, V.I. Bondarchuk, D.V. Oryshych, S.G. Sedov, and V.A. Golub, *Prog. Phys. Met.*,

24, No. 1: 75–105 (2023);
https://doi.org/10.15407/ufm.24.01.075
30. M.O. Vasylyev, B.M. Mordyuk, and S.M. Voloshko, *Prog. Phys. Met.*, **24**, No. 1: 5–37 (2023);
https://doi.org/10.15407/ufm.24.01.005
31. M.O. Vasylyev, B.M. Mordyuk, and S.M. Voloshko, *Prog. Phys. Met.*, **24**, No. 1: 38–74 (2023);
https://doi.org/10.15407/ufm.24.01.038
32. S. Schwab, R. Selin, and M. Voron, *Weld. World,* **67**: 981–986 (2023);
https://doi.org/10.1007/s40194-023-01464-z
33. S.V. Akhonin and S.L. Schwab, *Paton Weld. J.*, **2019**, No. 6: 34–37 (2019);
https://doi.org/10.15407/tpwj2019.06.06
34. V.P. Prilutsky, S.V. Akhonin, S.L. Schwab, and I.K. Petrychenko, *Mater. Sci. Forum*, **927**: 119–125 (2018);
https://doi.org/10.4028/www.scientific.net/msf.927.119
35. A.V. Zavdoveev, T. Baudin, D.G. Mohan, D.L. Pakula, D.V. Vedel, and M.A. Skoryk, *Prog. Phys. Met.*, **24**, No. 3: 561–592 (2023);
https://doi.org/10.15407/ufm.24.03.561
36. H.O. Pierson, *Handbook of Refractory Carbides & Nitrides: Properties, Characteristics, Processing and Applications* (Westwood, NJ, USA: Noyes Publications: 1996);
https://www.sciencedirect.com/book/9780815513926/handbook-of-refractory-carbides-and-nitrides#book-description
37. O.N. Grigoriev, A.V. Stepanenko, V.B. Vinokurov, I.P. Neshpor, T.V. Mosina, and L. Silvestroni, *J. Eur. Ceram. Soc.*, **41**, No. 9: 4720–4727 (2021);
https://doi.org/10.1016/j.jeurceramsoc.2021.02.053
38. D. Vedel, M. Storozhenko, P. Mazur, V. Konoval, M. Skoryk, O. Grigoriev, M. Heaton, and A. Zavdoveev, *Open Ceram.*, **15**: 100393 (2023);
https://doi.org/10.1016/j.oceram.2023.100393
39. M.D. Abramoff, P.J. Magalhaes, and S.J. Ram, *Biophotonics Int.*, **11**, No. 7: 36 (2004).
40. I.L. Shabalin, *Ultra-High Temperature Materials I* (Dordrecht: Springer: 2014);
https://doi.org/10.1007/978-94-007-7587-9
41. I. Spiridonova, A. Panasyuk, E. Sukhovaya, and A. Umanskiy, *Stability of Composite Materials* (Dnipropetrovsk: Svidler: 2011) (in Russian).
42. A.D. Panasyuk, V. Fomenko, and G. Glebova, *Resistance of Non-Metallic Materials in Melts* (Kiev: Naukova Dumka: 1986) (in Russian).
43. A.F. Lisovsky, *Migration of Metal Melts in Sintered Composite Bodies* (Kiev: Naukova Dumka: 1984) (in Russian).
44. A. Salmasi, S.J. Graham, I. Galbraith, A.D. Graves, M. Jackson, S. Norgren, D. Guan, H. Larsson, and L. Höglund, *Calphad*, **74**: 102300 (2021);
https://doi.org/10.1016/j.calphad.2021.102300
45. P.G. Clites and E.D. Calvert, *Laboratory-Scale Casting Furnaces for High-Melting-Point Metals* (Washington: US Department of the Interior Bureau of Mines: 1961).
46. P. Wanjara, R.A.L. Drew, J. Root, and S. Yue, *Acta Mater.*, **48**, No. 7: 1443–1450 (2000);
https://doi.org/10.1016/s1359-6454(99)00453-x
47. T.O. Mapoli, K.A. Annan, C.W. Siyasiya, and K. Mutombo, *IOP Conf. Ser.*, **655**: 012028 (2019);
https://doi.org/10.1088/1757-899x/655/1/012028
48. S.V. Prikhodko, P.E. Markovsky, S.D. Sitzman, M.A. Gordillo, J.M.K. Wiezorek, and O.M. Ivasishin, *Proceedings of the 13th World Conference on Titanium*

(Eds. V. Venkatesh, A.L. Pilchak, J.E. Allison, S. Ankem, R. Boyer, J. Christodoulou, H.L. Fraser, M. Ashraf Imam, and Y. Kosaka) (USA: The Minerals, Metals & Materials Society: 2016), Ch. 64, p. 415; https://doi.org/10.1002/9781119296126.ch64

49. H. Yu, Q. Fan, and X. Zhu, *Materials*, **13**, No. 17: 3886 (2020); https://doi.org/10.3390/ma13173886
50. P.E. Markovsky, D.V. Kovalchuk, J. Janiszewski, B. Fikus, D.G. Savvakin, O.O. Stasiuk, D.V. Oryshych, M.A. Skoryk, V.I. Nevmerzhytskyi, and V.I. Bondarchuk, *Prog. Phys. Met.*, **24**, No. 4: 741–763 (2023); https://doi.org/10.15407/ufm.24.04.741

Received 25.08.2023;
in final version, 30.10.2023

П.Є. Марковський[1], *Д.В. Ковальчук*[1,2],
С.В. Ахонін[3], *С.Л. Шваб*[3], *Д.Г. Саввакін*[1], *О.О. Стасюк*[1],
Д.В. Оришич[1], *Д.В. Ведель*[4], *М.А. Скорик*[1], *В.П. Ткачук*[1,2]

[1] Інститут металофізики ім. Г.В. Курдюмова НАН України,
бульв. Академіка Вернадського, 36, 03142 Київ, Україна
[2] ПрАТ НВО «Червона хвиля»,
вул. Дубровицька, 28, 04114 Київ, Україна
[3] Інститут електрозварювання ім. Є.О. Патона НАН України,
вул. Казимира Малевича, 11, 03150 Київ, Україна
[4] Інститут проблем матеріалознавства ім. І.М. Францевича НАН України,
вул. Омеляна Пріцака, 3, 03142 Київ, Україна

НОВИЙ ПІДХІД ДО ВИГОТОВЛЕННЯ МЕТАЛОМАТРИЧНИХ КОМПОЗИТІВ Ti–6Al–4V + 40% TiC 3*D*-ДРУКОМ ІЗ ВИКОРИСТАННЯМ КОНІЧНОГО ЕЛЕКТРОННОГО ПРОМЕНЯ ТА ПОРОШКОВОГО ДРОТУ. Ч. 1: ОСНОВНІ ОСОБЛИВОСТІ ПРОЦЕСУ, ФОРМУВАННЯ СТРУКТУРИ ТА ХАРАКТЕРИСТИКИ 3*D*-ДРУКОВАНОГО МАТЕРІАЛУ

В даній статті розглянуто новий метод виготовлення за адитивними технологіями металоматричного композиту на основі титанового стопу Ti–6Al–4V, зміцненого частинками карбіду Титану, а також шаруватих структур, що складаються з шарів вказаного композиту та стопу Ti–6Al–4V. Метод ґрунтується на 3*D*-друці з використанням електронного променя конічного профілю та спеціального порошкового дроту, склад якого відповідає металоматричному композиту. В роботі описано деталі виробництва такого дроту та процесу 3*D*-друку з його використанням, особливості формування мікроструктури та фазового складу друкованого композитного матеріялу. В додаткових експериментах розглянуто особливості змочування частинок карбіду Титану розтопом складу Ti–6Al–4V в процесі 3*D*-друку та можливі термоґравітаційні ефекти (спливання або опускання на дно розтопу) твердих частинок TiC. Показано вплив індивідуальних компонентів у складі дроту на формування мікроструктури та її однорідність у поперечному перерізі друкованого шару. Показано можливість формування однорідного структурного стану та досягнення достатньо високих значень твердости (вище 600 *HV*) шару металоматричного композиту, друкованого на плиті Ti–6Al–4V в якості підкладинки.

Ключові слова: адитивні технології, 3*D*-друк, титанові стопи, металоматричний композит, мікроструктура, текстура, твердість.